Multiscale simulation to predict microstructure dependent effective elastic properties of an injection molded polypropylene component

Contents lists available at ScienceDirect

Mechanics of Materials

journal homepage: www.elsevier.com

Multiscale simulation to predict microstructure dependent effective elastic properties of an injection molded polypropylene component

Gottfried Laschet [a, *], Marcel Spekowius [b], Roberto Spina [b, c], Christian Hopmann [b]

[a] ACCESS e.V. RWTH Aachen University, Intzestraße 5, D-52072, Aachen, Germany
[b] Institute of Plastics Processing (IKV), RWTH Aachenkita University, Aachen, Germany
[c] Department of Mechanics, Mathematics and Management (DMMM), Politecnico di Bari, Bari, Italy

ARTICLE INFO

Article history:
Received 12 October 2015
Received in revised form 20 October 2016
Accepted 25 October 2016
Available online xxx

Keywords:
Semi-crystalline polymers
Integrative multiscale simulation
Polymer crystallization
Two-level homogenization scheme
Injection molding

ABSTRACT

Industrial plastic parts, made of semi-crystalline polymers, are often produced by injection molding. In this process the melt undergoes a complex deformation and cooling history which results in an inhomogeneous distribution of spherulites in the component. The different size and shape of the spherulites induce local variations of the elastic properties in the final part. To evaluate these inhomogeneities in an isotactic polypropylene (α-iPP) component accurately, a 3D multi-scale, integrated simulation approach has been developed. At first, a coupled mold filling and heat transfer analysis is achieved at the macro-scale and the predicted velocity and temperature fields are transferred to the micromodel. Then, a 3-D microstructure evolution model is developed, where the nucleation of spherulite germs and their growth are described. To evaluate their effective mechanical properties a two-level homogenization scheme has been adopted. At the nano-scale, the effective properties of the lamella build of crystalline and amorphous phases are determined. In this study, not only the radial growing lamella of amorphous and crystalline phases is homogenized, but also its "cross hatched" lamellar structure. At the micro-scale, the spherulite microstructure is homogenized via a 3D radial distribution of equivalent lamellae around its mono-crystal center. Finally, the application of the developed homogenization scheme allows the prediction of the distribution of effective mechanical properties over the component thickness in different sections of the staggered component.

1. Introduction

The manufacturing of high quality injection molded parts requires a deep understanding of the link between material properties, process parameters and product design. The behavior of a semi-crystalline polymer during the injection molding process and the quality of the final part are significantly influenced by the microstructure formed during the filling and cooling process. In contrast to pure amorphous thermoplastics, the molecular chain of semi-crystalline polymers (SCP) is partly arranged in periodic patterns during solidification. During the solidification process, plate shaped arrangements of the molecules, called *lamellae*, develop through the folding of the polymer chains. These lamellae are built by the amorphous and crystalline phases, which have the same chemical but different physical properties. They are characteristic for most of the semi-crystalline polymers (Mischler and Baltra-Calleja, 2012). In the solidified melt, the lamellae can be arranged to superstructures of different shape, for instance in a radial configuration, named *spherulite*, or, in presence of highly oriented melt, to shish-kebab structures (Janeschitz-Kriegl, 2010). The radial superstructure appears mainly in PE and PP thermoplastics. The diameter of the spherulites varies from few microns up to several millimeters. This diameter depends, besides the considered material, on the local boundary conditions during solidification. During the injection molding process, the boundary conditions vary strongly so that the shape and size of the spherulite vary significantly as well (see Fig. 1). This inhomogeneity of the spherulites affects the properties of the component, which need to be determined accurately.

In order to predict valuable, local effective mechanical properties of an injection molded part, we have to develop not only a suitable homogenization scheme, which takes into account the lamella plate structure at the nano-scale and their radial distribution in each spherulite at the microscale, but also to link this homogenization scheme within an integrative, multiscale approach (see Fig. 2). At first, a coupled mold filling and heat transfer analysis has to be performed at the macro-scale in order to specify the local velocity and temperature fields.

These fields are extracted and transferred to the microstructure evolution simulation, which describes the crystallization process. The developed simulation model of the injection molding process is briefly reviewed in Section 2 and more detailed in references (Spina et al., 2014a, 2014b; Spekowius et al., 2016).

Concerning the crystallization process of SCP, the literature is broad. Yamamoto (2009) realizes an extensive review of such models and presents results for quiescent crystallization, under flow or large deformation, for different polymers. Raabe (2004) uses a cel-

* Corresponding author. Fax: +4904924138578.
Email address: g.laschet@access.rwth-aachen.de (G. Laschet)

http://dx.doi.org/10.1016/j.mechmat.2016.10.009
0167-6636/

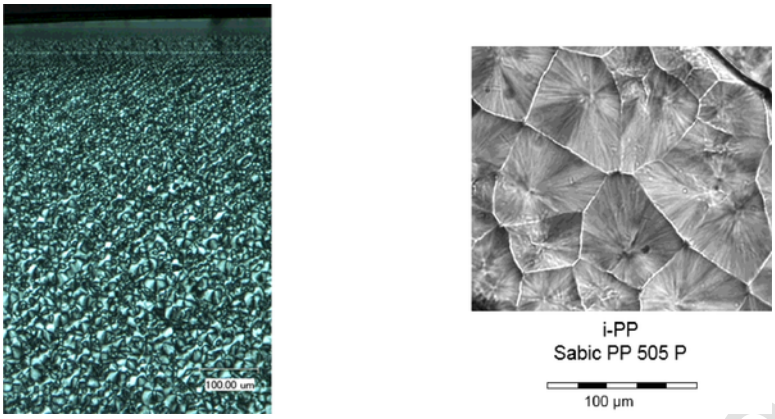

Fig. 1. Light microscopies of α-iPP microstructures produced by injection molding. Large spherulites are observed in the plate core (bottom); whereas fine spherulites are located behind an amorphous skin layer (top). On the right microstructure zoom, thin interfaces between spherulites are identified.

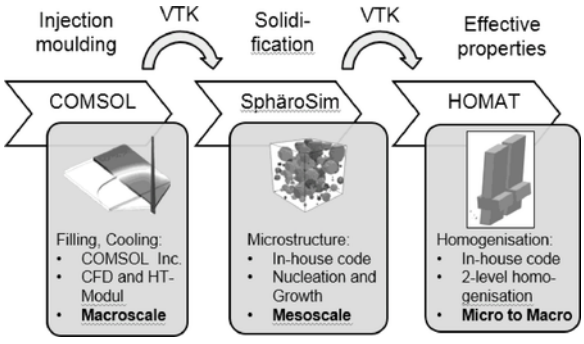

Fig. 2. Multiscale simulation chain in order to predict microstructure dependent effective material properties.

lular automaton to calculate the growth of spherulites in a polymer melt under quiescent conditions. Later, he extended his model to consider also weak shearing (Raabe and Godora, 2005). Charbon and Swaminarayan (1998) calculate spherulite formation in a temperature field using a front tracking method. Pantani et al. (2005) analyze the effect of the injection molding process on the crystallization process. They implement a quiescent crystallization model to predict the morphology after the injection process and show that simulations neglecting the flow effect on the crystallization process leads to too large spherulites, not observed in the experiment. Our research goal is to compute the local microstructure evolution up to a scale of few microns by taking into account not only thermally induced quiescent nucleation but also flow induced nucleation via the reptation model of Doi and Edwards (1988) and to describe the spherulite growth speed via the Hoffman et al. (1976) model. The developed microstructure model, detailed in Spekowius et al. (2016), is briefly outlined in Section 3. It differs also from the previous developed model in Michaeli et al., 2012, where only thermally induced quiescent nucleation is taken into account and the flow induced contribution is there neglected.

Semi-crystalline polymers, such as isotactic PP or polyethylene (PE) are considered in the literature as heterogeneous materials and mean-field micromechanical models like Lee et al. (1993) and Van Dommelen et al. (2003) have been developed to predict their large strain elasto-viscoplastic behavior. Very little work has been done at the small strain level (Nikolov et al., 2002). Bédoui et al. (2006) have developed two specific micro-models for their elastic behavior, where either the crystalline phase or a two-phase inclusion are dispersed in the amorphous phase randomly. Gueguen et al. (2010) develop a three-phase model by a generalization of the double-inclusion model. They distinguish the tied amorphous phase, which is in direct contact with the crystalline phase, from the free amorphous phase around the lamellae. In their large strain model Brusselle-Dupend and Cangémi (2008) distinguish also the tied amorphous phase, which is viscoplastic, from the free amorphous phase, which remains elastic. Uchida and co-workers (Uchida et al., 2010; Uchida and Tada, 2013) present a nano-, micro- to macroscopic modelling of the viscoplastic deformation behavior of semi-crystalline PE. In their multiscale approach a laminar composite model and a finite element based homogenization method are used to relate the mechanical behavior of SCP from the nano- to the micro-scale and an isotropic spherulite model is introduced to perform the link between the micro- and the macro-scale. Recently, Oktay and Gürses (2015) develop a dedicated 2.5D spherulite model for polyethylene (PE) and perform the characterization of their micromechanical deformation by using a viscoplastic crystal plasticity model for the crystalline phase.

To our knowledge, only in our previous publications (Michaeli et al., 2012; Laschet et al., 2012) the crystallization results are used as direct input to predict the effective mechanical properties of SCP. In Michaeli et al. (2012), the asymptotic homogenization method is applied directly to the spherulites, assembled in few classes according to their crystallinity degree; whereas in Laschet et al. (2012) a first variant of the two-level homogenization scheme has been presented. Our goal here is to improve this scheme by taking the crimping of the molecular chain into account in the derivation of the crystalline phase, by modelling the twisting and the branching of lamellae, observed experimentally by Li et al, (2001) and by revisiting the radial spherulite model. In contrast to the initial model (Laschet et al., 2012), where each lamella orientation is specified randomly, here only the first lamella orientation of a spherulite is chosen randomly, all other orientations will be define in a deterministic way, as outlined in Section 4. Moreover, this section reports also the derivation of the amorphous and crystalline phase properties and the definition of the different RVE designs of the lamellae. Finally, in Section 5 the developed integrative multiscale simulation procedure is used to predict the variation of the effective elastic properties over the thickness in two sections of a staggered α-iPP plate.

2. Simulation of the injection molding process

In the multiscale simulation of effective material properties, the first important step is to simulate is the manufacturing process. It plays a major role as it defines the temperature and the pressure un-

der which the thermoplastic melt solidifies. For the simulation of the injection molding process the flow and cooling behavior of the melt has to be calculated accurately. Thereby many factors as the unsteady melt flow with a moving flow front, the contact between the non-Newtonian viscoelastic melt and the air inside the cavity, the phase change during the process and the heat transfer at the mold wall have to be considered. The complexity rises if 3D flows in complex geometries have to be calculated.

The description of incompressible viscous Navier–Stokes flows is based on the equations of mass, momentum and energy conservation. Let Ω denote the physical domain, then the following equations are valid within Ω:

$$\nabla \cdot \boldsymbol{u} = 0 \tag{1}$$

$$\rho \left(\frac{\partial \boldsymbol{u}}{\partial t} + \boldsymbol{u} \cdot \nabla \boldsymbol{u} \right) = -\nabla p + \nabla \cdot \underline{\tau} + \boldsymbol{F_{ext}} \tag{2}$$

$$\rho c_p \left(\frac{\partial T}{\partial t} + \boldsymbol{u} \cdot \nabla T \right) = \nabla \cdot (k \nabla T) + \underline{\tau} : \nabla \boldsymbol{u} + \rho \xi_{\max}^{abs} \Delta H_c \frac{\partial \xi}{\partial t} \tag{3}$$

with the velocity field **u,** the density ρ, the pressure p, the viscous stress tensor $\underline{\tau}$, the external forces $\boldsymbol{F_{ext}}$, the temperature T, the thermal conductivity k, the latent heat of crystallization ΔH_c, the relative degree of crystallization ξ and the absolute maximum degree of crystallization $\xi_{\max}^{abs}$. The relative degree of crystallinity on the macroscale is calculated using a simple Kolmogorov-Avrami–Evans approach, combined with the rate of crystallization by Nakurama et al. (1973), according to the following equations:

$$\xi = 1 - \exp\left[-K(T)\, t\right]^n \tag{4}$$

$$\frac{\mathrm{d}\xi}{\mathrm{d}t} = nK(T)(1-\xi)\left[-ln(1-\xi)\right]^{\frac{n-1}{n}} \tag{5}$$

where the degree of crystallization ξ is a function of the Avrami exponent n and of the overall non-isothermal kinetic rate constant $K(T)$.

The macro-scale description of the degree of crystallization is necessary to take into account the influence of the heat of crystallization on the local temperature. Of course, it has not the accuracy as it can have within the microstructure simulation on the microscale. However, investigations by Spina et al. (2014a) showed that the calculated crystallization degrees are sufficient accurate to be used in macroscale models. In addition to the influence on the temperature, the degree of crystallization $\xi$is also used in the description of thermophysical properties via expression:

$$f = f_{\mathrm{cryst}} \cdot \xi \cdot \xi_{\max}^{\mathrm{abs}} + f_{\mathrm{amorph}} \cdot \left(1 - \xi \cdot \xi_{\max}^{\mathrm{abs}}\right) \tag{6}$$

where f is a general thermos-physical property (e.g., the heat capacity or the thermal conductivity). Eq. (4) is a simple mixture rule of the pure phase properties (e.g. amorphous f_{amoprh} and crystalline f_{crys}). For a semi-crystalline polymer, like α-iPP, ξ ranges from 0 to 1; whereas the absolute maximum crystallization degree ξ_{max}^{abs} is dependent on the cooling rate. Under ideal conditions, the value ξ_{max}^{abs} is equal to zero for very high cooling rates, whereas for very low cooling rate is equal to 1. However, the value of ξ_{max}^{abs} under real process conditions is equal to 0.53 because the crystalline and amorphous phases coexist in a semi-crystalline material. Note that these properties are not the finally calculated effective properties, expressed via the developed multi-scale simulation approach. They do not take the local spherulite distribution into account. In addition, some material properties cannot be computed by this simple mixture rule. In particular, the density is not expressed via Eq. (6) but via a cooling rate dependent, modified 2-domain Tait model. The viscosity of the melt is also computed via a specific model, in which the entanglement effects of the molecular chains are neglected. The melt viscosity is linked with the stress tensor via expression:

$$\eta = \eta_{amorph} \cdot \left(1 - \frac{\xi \cdot \xi_{\max}^{abs}}{\varphi_{sph}}\right)^{-B\varphi_{sph}} \tag{7}$$

whereby the amorphous viscosity η_{amorph} is described by a simple cross-LF approach and B is the Einstein coefficient. B and φ_{sph} are fitting parameters, which take implicitly the spherulite volume into account.

In addition to the pure polymer flow, the multiphase aspect of the flow problem must be considered well. For this, the domain Ω is divided into sub-domains Ωi. One subdomain is created for the initially presented air in the cavity, one for the plastic melt. The progression of the flow front is described by an iso-surface with a distance function that describes the distance between the air and the melt (Osher and Sethian, 1988). This iso-surface is calculated by means of the level-set method in which the phase variable ϕ describes the current phase state. In the case of $\phi > 1/2$ there is locally polymer melt and for $\phi > 1/2$ air. The flow front simply is defined by $\phi > 1/2$. The temporal evolution of the flow front is given in the shared domains Ω_{melt} and Ω_{air}, according to Olsson and Kreiss (2005):

$$\frac{\partial \phi}{\partial t} + \boldsymbol{u} \cdot \nabla \phi = \kappa_S \nabla \cdot \left[\varepsilon \nabla \phi - \phi (1-\phi) \frac{\nabla \phi}{|\nabla \phi|} \right] \tag{8}$$

The parameter ε describes the thickness of the transition region between the two fluids, and $\kappa_S$denotes a stabilization term.

The Eqs. (1)–(8) have been implemented in the CFD (Computational Fluid Dynamics) and the HT (Heat Transfer) modules of the multiphysics finite element program COMSOL (2014). After the definition of the boundary conditions, which include the temperatures and velocities at the borders of the domains Ω_{i}, the velocity, the temperature, the pressure and the flow front curve are calculated. Note that the information about the material parameters used in the COMSOL model as well as the friction and interface heat transfer coefficients are reported in Spina et al. (2014b).

Finally, the calculated flow and temperature fields were converted into the VTK file format of the open source visualization toolkit Paraview (2014) and transferred to the microstructure evolution model (see Fig. 2). Note that the calculated pressure profiles are neglected in the further simulation of the crystallization process. This is due to the fact, that at the microscale the melt is assumed to be incompressible.

3. Simulation of the microstructure evolution

The calculation of the solidification process and the prediction of the resulting microstructure constitute the second step in the simulation chain (see Fig. 2). Here the method of the cellular automata was used, whereby the phase state of a small melt volume depends on the state of the adjacent volumes. This requires the definition of a Representative Volume Element (RVE) and its subdivision into a high-resolution mesh of voxels (Wienke et al., 2013). Each hexahedron describes a small melt volume with typical sizes of 1 µm³ to 1000 µm³, whose boundary conditions (temperature and flow field) are calculated from interpolations of the previously calculated temperature and velocity fields at the corner nodes of the RVE. The temperature is interpolated linearly and the velocity fields are interpolated using B-splines. The phase state of each voxel is described by a binary value which is zero for the liquid phase and one for the solid phase. Goal of the microstructure evolution model is the computation of the phase state evolution.

The simulation of the solidification process is based on an event-based methodology. Hereby, the nucleation and the growth events are distinguished. The tasks of the nucleation and the growth model are to calculate the time at which the events occur. Hereby a nucleation model based on a theory of Lauritzen and Hoffmann (1960) is adopted:

$$\dot{N} = Ck_BT\Delta G \exp\left(-\frac{Q}{kT}\right)\exp\left(-\frac{K_n}{T\Delta G^n}\right) \tag{9}$$

where $\dot{N}$ is the nucleation rate, which indicates the number of new nuclei per time and volume, C is a material-specific constant, k_B the Boltzmann constant, Q the activation energy of the nucleus, ΔG the Gibbs free energy per unit volume and K_n a material constant describing the geometry of the nucleus. The exponent n takes the values 1 or 2, depending on the temperature regime in which the nucleation occurs. The model parameters C, Q, n and $K_n$can be calibrated by means of isothermal experiments; whereas T is known via the boundary conditions and interpolated between the corner points of the microscale mesh. Only the Gibbs free energy ΔG needs to be calculated by microscopic models. In the present approach the Gibbs free energy is composed of a purely temperature-dependent term, characterizing quiescent nucleation, and a flow-dependent term: $\Delta G = \Delta G_q + \Delta G_f$. This Gibbs energy decomposition constitutes a clear improvement of the previous model (Michaeli et al., 2012), which neglects the flow dependent contribution. The quiescent term ΔG_q can be easily derived from steady state conditions by:

$$\Delta G_q = \Delta H_c \cdot \left(1 - \frac{T}{T_{m,0}}\right) \tag{10}$$

where $T_{m,0}$ corresponds to the equilibrium melting temperature.

The flow-dependent part ΔG_f has to be calculated by taking into account the polymer-polymer interaction. It exists different approaches to reflect this interaction in the simulation; one of these approaches is the reptation model of Doi and Edwards (1988). The neighboring polymers of a polymer chain are considered as obstacles that confine the cylindrical area in which a polymer chain can move freely (see Fig. 3). Based on this observation, functions can be set up that describe the influence of the flow field on a polymer chain, leading to the following expression for the flow induced contribution to the Gibbs free energy (Coppala et al., 2001):

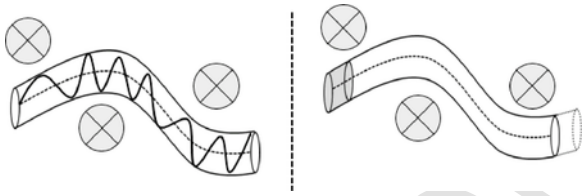

Fig. 3. Reptation model of Doi and Edwards for the polymer-polymer interaction in flow dependent melts. Left: polymer chain confined in a cylindrical shape. Right: movement of the chain in a creeping manner.

$$\Delta G_f = \frac{3ck_BT}{4\pi}\int_{-\infty}^{t} dt'\dot{\mu}\left(t,t'\right)\int d\boldsymbol{u}\ln\left(\left|\boldsymbol{E}\left(t,t'\right)\cdot\boldsymbol{u}\right|\right) \tag{11}$$

where $\mu(t, t')$ is the memory function of Doi and Edwards, c the entanglement, $\boldsymbol{E}(t, t')$ defines the deformation tensor of the chain between the times t' and t and $\boldsymbol{u}$ is a unit vector.

The non-linear viscoelastic behavior of the plastic melt and thus the interaction between the polymer chains are described by following memory function $\mu(t, t')$:

$$\mu(t) = \frac{8}{\pi^2}\sum_i \frac{1}{i^2}\exp\left(-\frac{i^2 t}{\tau_d}\right) \tag{12}$$

The sum is executed only for odd values of i. The material parameter τ_d, named disengagement time, describes the relaxation behavior of the polymer. This parameter is linked to the molecular weight of the entanglement M_e and to the zero shear viscosity $\eta_0(T)$ by:

$$\tau_d = \frac{20}{\pi^2}\frac{M_e}{RT\rho_{melt}}\eta_0(T) \tag{13}$$

The zero shear viscosity can be easily determined via rheological measurements. Thus, the disengagement time τ_d can be expressed by quantities, measured at the macroscale. This is a clear advantage of the implemented reptation model.

The integration of the nucleation rate (9) allows the computation of the number of active nuclei per unit volume at any time, $N_V(t)$. By choosing the integration intervals small enough, this number can be used in a Monte–Carlo step of the developed Cellular Automaton to calculate the spatial distribution of active nuclei by comparing $N_V(t)$ to an uniformly distributed random number R (see Spekowius et al., 2016). The nucleation model depends on the local temperature and velocity field which are computed in the macroscale simulation (see Eqs. (1)–(3)). As these fields change over time and location, there is also a locally varying nucleation rate and thus spherulite nucleation. Based on this nuclei repartition at a given time in the RVE, the crystal growth is simulated. Only the radial growth is taken into account, since this growth type describes the formation of spherulites. The crystal growth can be described with the Hoffman, Davis and Lauritzen model (1976) in which a layer growth process is computed by averaging the nucleation process on an existent surface:

$$v_G = v_0\exp\left(-\frac{U^*}{R\left(T-T_\infty\right)}\right)\exp\left(-\frac{\kappa_G T_{m,0}^2\left(T_{m,0}+T\right)}{2T^2\left(T_{m,0}-T\right)}\right) \tag{14}$$

Here, the term $\exp\left(-\frac{U^*}{R(T-T_\infty)}\right)$ describes the temperature dependence of the rate at which new polymer chain segments solidifies. The temperature T_∞ corresponds to a hypothetical temperature at which no movement of the molecular chains exists. This temperature varies from material to material and is usually 30–60 K below the glass transition temperature. κ_G and v_0 are material parameters, which in accordance with experimental measurements, can be considered as constant parameters.

Currently, two algorithms are implemented in the in-house code, SphaeroSim, for the calculation of the crystal growth process (see Fig. 4):

- Monte–Carlo method (Raabe, 2004): for each cell in the crystal growth front a probability is calculated and converted to a phase change in a Monte–Carlo step.
- Ray tracing algorithm: for each cell in the growth front a time for phase change is calculated by integrating the growth front along a path starting in the spherulite center. To perform this integration, the intersection points with the cell boundaries are determined. The time to achieve phase change of a cell is determined when the front reaches the far side intersection point of the cell.

One evident difference between the two algorithms used for the simulation of the crystal growth was the final spherulite shape. In fact, the stochastic nature of the Monte–Carlo method leads to spherulite shapes which are not smooth. The ray tracing algorithm has no random number contribution and thus leads to obviously smoother spherulites (Spekowius et al., 2016). This method, which is more time consuming as it involves numerical path integration, will be used here as precise forecast of the spherulite shape, if desired. Neglecting flow and athermal influences is a simplification which is often sufficient (see e.g. Koscher and Fulchiron, 2002 or Lee and Kamal, 1999). However, it is questionable how general this simplification holds. A consideration of flow on the crystal growth would require a micro description of the crystallization only with a nucleation model. This would dramatically increase the computational time as the layer averaging used in the growth model cannot be applied anymore.

Together, the nucleation and the growth model allow the calculation of the evolution of the spherulite microstructure during the solidification process. Application results are presented in Section 5. In a final step, the boundaries between individual spherulites are marked as interface layers in order to be considered as an individual phase in the subsequent calculation of the effective mechanical properties. The so calculated final microstructure is exported to the homogenization tool HOMAT (Laschet and Apel, 2010; Laschet et al., 2012) via the standardized VTK exchange format.

4. Homogenization of semi-crystalline thermoplastics

The third and last step of the simulation chain is the calculation of the effective mechanical properties of the previously determined inhomogeneous microstructure of the SCP. These thermoplastics are built at the microscale by an agglomeration of spherulites, which are separated by a thin interface layer (see Fig. 1 right). Each spherulite grows radially from its mono-crystalline nucleus and consists of twisted lamellae of crystalline and amorphous phases. Each crystalline part of such lamella corresponds to a folded molecular chain, which for the isotactic PP is helicoidal (see Fig. 5). As shown by Li et al. (1999), secondary nucleation on a lamella can occur during spherulite growing as well as joining of two lamellae (see Fig. 6).

This brief zoom through the scales of an isotactic PP describes the complexity of its microstructure, which has to be homogenized accurately. Additionally, the fact that the amorphous and crystalline phases are not separable increases the challenge for the homogenization scheme. Indeed, it is not possible to produce bulk specimens of pure crystalline and pure amorphous phases. Therefore, an individual characterization of the mechanical properties of each phase is not possible, so that their determination is delicate.

4.1. Mechanical properties of the amorphous and crystalline phases

In order to get the mechanical properties of the amorphous phase of α-iPP, we follow Bédoui et al. (2006), who assume that at the room temperature this phase is *isotropic* and in a *rubbery-elastic* state. The shear modulus G of this phase is related to the molecular mass between entanglements M_e by following relation: $G_{amoph} = \rho RT/M_e$, where ρ is the amorphous phase density, T the temperature and R the ideal gas constant. The value of M_e is set to 7 kg/mol (Fetters et al., 2007). This leads to $G_{amorp} = 0.3$ MPa and consequently to $E_{amorph} = 0.9$ MPa. The amorphous phase is *quasi-incompressible* with a Poisson coefficient of $\nu = 0.49993$. These elastic, rubber-like properties specifies following Hooke matrix for the

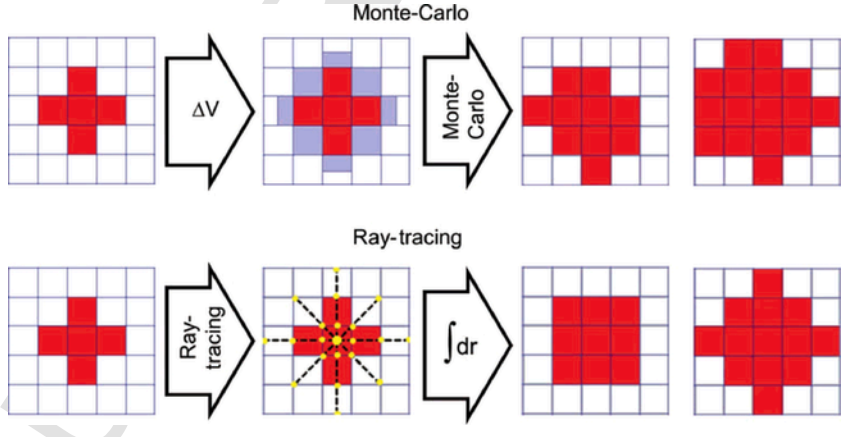

Fig. 4. Illustration of the Monte–Carlo approach (top) and of the ray-tracing algorithm (bottom).

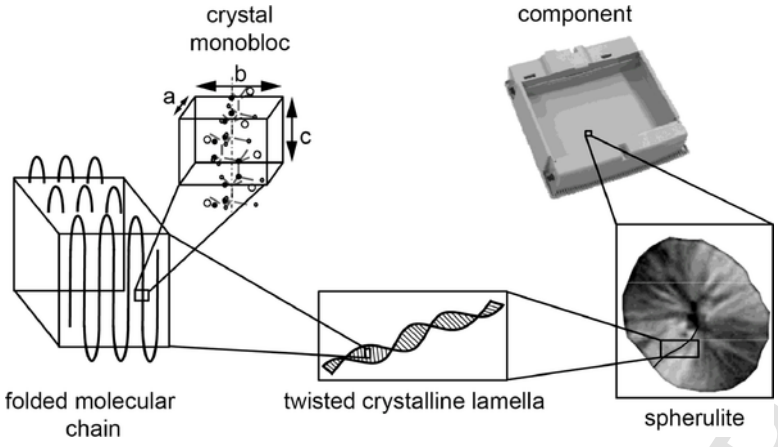

Fig. 5. Zoom in the morphological composition of an isotactic polypropylene component.

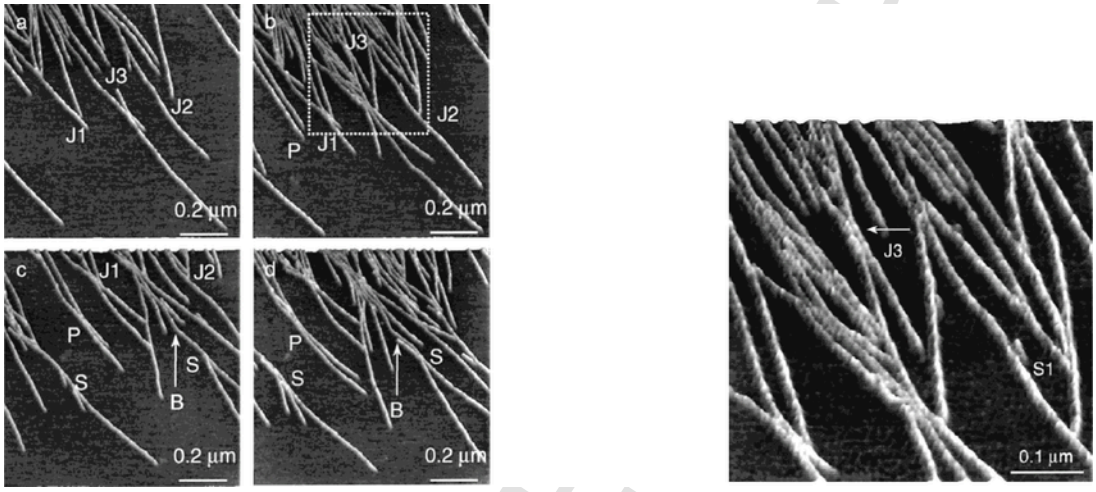

Fig. 6. Growth of lamellae and spherulites of a semi-crystaline polymer by AFM (Li et al., 1999). Left: J2 = joining of a growing lamella with an existing lamella. J3 = joining of opposite growing lamellae. S = branching of lamellae by secondary nucleation and B = bending of a lamella. Right: zoom of area around J3 with S1 = start of daughter lamella embryo.

pure amorphous phase:

$$H_{amorph} = \begin{bmatrix} 2143.3 & 2142.7 & 2142.7 & 0 & 0 & 0 \\ & 2143.3 & 2142.7 & 0 & 0 & 0 \\ & & S & 2143.3 & 0 & 0 & 0 \\ & & & Y & 0.3 & 0 & 0 \\ & & & & M & 0.3 & 0 \\ & & & & & & 0.3 \end{bmatrix} \quad (15)$$

To derive the mechanical properties of the crystalline phase, we start with the theoretical Hooke matrix of Tashiro et al. (1992), obtained by molecular dynamics simulations. Their results outlined the significant 3-D anisotropy of the Young modules of the crystalline phase, due to the important anharmonic torsional vibrational modes of the methyl groups. Their Hooke matrix defines the basis of the derived monoclinic Hooke matrix for the pure crystalline phase (see Eq. (16). Indeed, this phase presents only one symmetry plane perpendicular to the molecular chain (direction c in Fig. 7 left) and the predicted Young modulus in chain direction is very high: 42,440 MPa.

However, these are idealized properties of a mono-crystalline straight α-iPP molecular chain. But, in spherulites and even in ultra-high strength drawn PP films, there always exists an interface with tied amorphous molecules. Kamazewa et al. (1979) used a simple composite model of serial and parallel connection of tied amorphous and crystalline region to link the apparent Young modulus to the pure crystalline one. Based on the X-ray diffraction measurements of Sawatari and Matsuo (1986) and using Kamezawa et al.'s approach, an apparent chain modulus of $E_c = 21{,}240$ MPa is derived. This value was used in our previous simulations (Laschet et al., 2012), but it neglects the fact that the molecular chain is folded in a crystalline phase (see Fig. 7 right).

In order to take into account the crimping of the molecular chain in a simplified way, two chain parts are distinguished: the straight one with E_c as Young modulus and the folded part, having a reduced Young modulus of $E_c/4$. Note that the analogy between the stiffness of a folded chain with a woven yarn is used here in order to specify the adopted reduction factor (Ivanov et al., 2010). By assuming that both folded parts have a volume fraction of $v_f = 0.3$, we get the following serial mixture rule:

$$E_3 = 0.7E_c + 0.3 \cdot \frac{E_c}{4} = 0.775E_c = \mathbf{16,460}\ MPa.$$

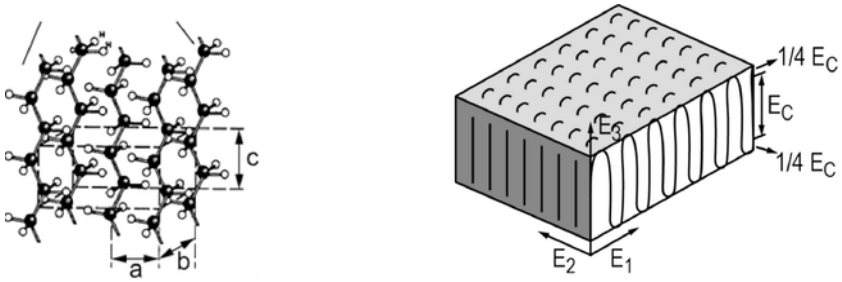

Fig. 7. Left: the crystalline monobloc of isotactic PP at the atom scale. Right: folding of the molecular chain in the growing direction and definition of the local axis system (E_1, E_2, E_3).

Moreover, as the packing of the folded chains is higher in the growth direction E_1 than in the perpendicular direction E_2, due to larger molecular forces in direction E_1, the corresponding stiffness is also higher. Therefore, we adopt a Young modulus E_1, which is 40% larger than E_2. All these considerations and assumptions are incorporated in the following Hooke matrix of the crystalline phase, expressed in the local axis system (E_1, E_2, E_3):

$$H_{crys} = \begin{bmatrix} 4340 & 1290 & 1320 & 0 & -120 & 0 \\ & 2810 & 1230 & 0 & 300 & 0 \\ & S & \mathbf{16,460} & 0 & -190 & 0 \\ & & Y & 1410 & 0 & -40 \\ & & & M & 1460 & 0 \\ & & & & & 1650 \end{bmatrix} \quad (16)$$

This Hooke matrix improves the theoretical stiffness tensor of Tashiro et al. (1992) for the crystalline phase.

4.2. Two-level homogenization scheme

A spherulite has essentially a quasi-radial distribution of twisted crystalline lamellae and of amorphous molecules between them (see Fig. 8) around its mono-crystal nucleus. As the nano- and the micro-scales can be separated, we introduce therefore firstly in Laschet et al. (2012) a two-level homogenization scheme for semi-crystalline thermoplastics such as for the isotactic PP:

- *Nanoscale*: homogenization of the lamellae formed by the crystalline phase and the amorphous layer taking or not possible branching due to secondary nucleation and or lamellae joining into account;
- *Microscale*: homogenization of the polyspherulite microstructure with thin interfaces between the individual spherulites. In each spherulite a radial distribution of equivalent lamellae around its mono-crystal center is assumed.

To perform these two homogenization steps, a first order homogenization scheme, based on an asymptotic expansion method (Sanchez-Palencia, 1980) is used. This method, detailed elsewhere (e.g. in Laschet and Apel, 2010), is briefly summarized hereafter.

Fig. 8. Left: 3D spherulite observed by atomic force microscopy (AFM). Right: lamellae in an α-iPP spherulite (Bédoui et al., 2006).

4.3. The asymptotic homogenization method

This method starts with a formal asymptotic expansion of the periodic displacement and temperature fields, $\mathbf{u}^h$ and T^h with the scale ratio ε, defined by $\mathbf{y} = \mathbf{x}/\varepsilon$ on the Representative Volume Element (RVE) of the heterogeneous material:

$$\begin{aligned} \mathbf{u}^h(\mathbf{x},\mathbf{y}) &= \mathbf{u}^0(\mathbf{x},\mathbf{y}) + \varepsilon\,\mathbf{u}^1(\mathbf{x},\mathbf{y}) + \mathrm{O}\left(\varepsilon^2\right) \\ T^h(\mathbf{x},\mathbf{y}) &= T^0(\mathbf{x},\mathbf{y}) + \varepsilon T^1(\mathbf{x},\mathbf{y}) + \mathrm{O}\left(\varepsilon^2\right) \end{aligned} \quad (17)$$

where $\mathbf{x}$ expresses *the macroscopic, global variable*, which measures the low variation of the mean value of the considered property from RVE to RVE; whereas $\mathbf{y}$ specifies *the periodic microscopic variable*, which describes the strong variation of the property within each RVE.

The scale ratio ε has a small value and depends if we consider the nano- to microscale transition or the transition between the micro- and the macroscale. The Hooke matrix of the heterogeneous lamella or of the semi-crystalline polymer is assumed to be a periodic function, whose first order asymptotic expansion is given by:

$$H^h_{ijkl}(\mathbf{y},T) = H^0_{ijkl}\left(\mathbf{y},T^0\right) + \varepsilon\,T^1(\mathbf{y})\,\frac{\partial H_{ijkl}}{\partial T} + \mathrm{O}\left(\varepsilon^2\right) \quad (18)$$

The serial developments (17) and (18), the differential operator $\frac{D}{DZ_i} = \frac{\partial}{\partial x_i} + \frac{1}{\varepsilon}\frac{\partial}{\partial y_i}$ and the following stress definitions:

$$\begin{aligned} S^r_{ij} &= H_{ijkl}\left(\mathbf{y},T^0\right).E_{kl}(\mathbf{u}^r) \qquad \textit{macroscopic stress} \\ s^r_{ij} &= H_{ijkl}\left(\mathbf{y},T^0\right).e_{kl}(\mathbf{u}^r) \qquad \textit{microscopic stress} \end{aligned} \quad (19)$$

where $\mathbf{u}^r$ specifies either $\mathbf{u}^0$ or $\mathbf{u}^1$ and E_{kl} and e_{kl} are *the macroscopic and microscopic strains* expressed either in terms of $\mathbf{x}$ or $\mathbf{y}$ respectively (Laschet and Apel, 2010); are introduced in the static equilibrium equations $\frac{D}{DZ_j}\sigma^h_{ij} + b_{i=0}$ leading to a system of differential equations, sorted with respect to the scale ratio ε:

$$1.\quad \varepsilon^{-2}\,\text{term}: \qquad \frac{\partial}{\partial y_j}s^0_{ij}(\mathbf{x},\mathbf{y}) = 0 \quad (20)$$

These differential equations are homogeneous. As the Hooke matrix is positive definite, $e_{ij}(\mathbf{u}^0) = 0$ and $u^0(\mathbf{x},\mathbf{y}) = u(\mathbf{x})$. Thus, the first term of the serial expansion, $\mathbf{u}^0$, depends only on the macroscopic variable **x** and not on the microscopic one.

$$2.\quad \varepsilon^{-1}\,\text{term}: \qquad \frac{\partial}{\partial y_j} S_{ij}^0(\mathbf{x},\mathbf{y}) + \frac{\partial}{\partial y_j} s_{ij}^1(\mathbf{x},\mathbf{y}) = 0 \tag{21}$$

This system is linear in **y**. Its solution is composed of the homogeneous solution: $u^1(\mathbf{x},\mathbf{y}) = \bar{u}^1(\mathbf{x})$ plus a special solution of type:

$$u_i^1(\mathbf{x},\mathbf{y}) = -\zeta_i^{rs}(\mathbf{y})\, E_{rs}^0(\mathbf{x}) \tag{22}$$

where $\zeta^{rs} = \left[\zeta_x^{rs}, \zeta_y^{rs}, \zeta_z^{rs}\right]$ with rs = xx, yy, zz, xy, xz, yz are periodic microscopic displacement fields induced by the initial macrostains $E_{rs}^0(\mathbf{x})$, which are taken unitary in elasticity.

At next, the special solution (22) is introduced in the system (21) and then the initial macrostrains $E_{rs}^0(\mathbf{x})$ are extracted from the system, leading to following system:

$$\frac{\partial}{\partial y_j} H_{ijrs}(\mathbf{y}, T^0) = \frac{\partial}{\partial y_j}\left[H_{ijkl}(\mathbf{y}, T^0)\, e_{kl}(\zeta^{rs})\right] \tag{23}$$

A variational formulation is applied to the differential system (23) in order to determine the unknown displacement fields ζ^{rs} (Guedes and Kikiuchi, 1999). Using a 3D finite element discretization of the RVE, the nodal values $\mathbf{Z}^{rs}$ of these fields are solution from the following discretized RVE problems (see e.g Laschet and Apel, 2010):

$$\mathbf{K}(T^0) * \mathbf{Z}^{rs} = \mathbf{g}^{im,H} + \mathbf{g}^{\Delta H} \tag{24}$$

where:

- $\mathbf{K}(T^0)$ is the elastic stiffness matrix of the RVE;
- $\mathbf{g}^{im,H}$ are implicit surface tractions, which are induced by the jump of the Hooke matrix at the phase boundaries;
- $\mathbf{g}^{\Delta H}$ are implicit body forces, which are induced by the variation of the Hooke matrix within each material phase of the RVE.

3. ε^0 term: The solution of this term leads to the definition of following effective Hooke matrix of the considered heterogeneous material:

$$H_{ijkl}^{hom}(T^0) = \frac{1}{|Y|}\int_Y \left[H_{ijkl}(T^0,\mathbf{y}) - H_{ijrs}(T^0,\mathbf{y})\, .\, e_{rs}(\zeta^{kl})\right] dy$$

where T^0 is the mean temperature on the RVE, |Y| the volume of the RVE and $e_{rs}(\zeta^{rs})$ the microscopic total strains.

Note that expression (25) constitutes an improvement of the volume averaging Hooke matrix, given simply by the first term of Eq. (25).

Eventually, in order to get the effective engineering properties, the predicted Hooke matrix (23) is symmetrized and then inverted. From the obtained flexibility matrix $\mathbf{S}_{ijkl}^{hom}$, the effective orthotropic Young modules (E_X, E_Y, E_Z), and shear modules (G_{XY}, G_{XZ}, G_{YZ}) and the effective Poisson coefficients (ν_{XY}, ν_{XZ}, ν_{YZ}) are derived in the RVE axis system ($\mathbf{e}_X$, $\mathbf{e}_Y$, $\mathbf{e}_Z$) (Nemat-Nasser and Hori, 1999).

4.4. Homogenization of the crystalline/amorphous lamella at the nanoscale

In a lamella the spatial distribution of the amorphous and crystalline phase has to be defined on the nanoscale. The goal is to design the best possible approximation of the lamellar structure within spherulites of an injection molded specimen. In particular, the proportion of the pure crystalline phase has to correspond to the degree of crystallization $\xi = 53\%$, measured by differential scanning calorimetry. Based on SEM micrographs of α-iPP in Mischler and Baltra-Calleja (2012, page 259) and observations of Bédoui et al. (2006), the geometry of a plane unit cell, named crux2D, is specified (see Fig. 9). The mean length of the lamella is set to 1500 nm and the width of the crystalline phase w_c to 60 nm; whereas the width of the amorphous phase (w = 65.2 nm) respects $\xi = 53\%$. Moreover, the α-iPP lamella is twisted by angle of nearly 6° over the specified length (Assoiline et al., 2001). To simply model the lamella twist, we define an equivalent flat crux2D design with a larger thickness of 21.6 nm instead of the initial 15 nm. In this design the volume fraction of each phase and the global lamella volume are well respected.

The plate-like crux2D design improves the previous simple bi-lamella models (Laschet et al., 2012) not only by modelling the lamella twist but it allows also a proper application of the periodic boundary conditions in the $\mathbf{E}_1$–$\mathbf{E}_2$ plane (see Fig. 7.right) and a better fixation of the rigid body modes. The last two points are important as they affect the quality of the numerical homogenization results directly. Indeed, the homogenization of a lamella composed of an incompressible, low stiff amorphous phase with a highly anisotropic crystalline phase is a challenging numerical task. Special mixed finite elements with area bubble functions (Mahnken et al., 2008) are used to handle with the quasi-incompressibility of the amorphous phase.

In a second, more complex design, named skew3D, the formation of branches due to secondary nucleation is integrated firstly in a lamella design (see Fig. 10). The basis of this new design constitutes the design crux2D.

Castelein et al. (1997) measured by scanning force microscopy that the new branches formed an angle of 80.4° with the principal lamella direction. This constraint is taken into account as well as an

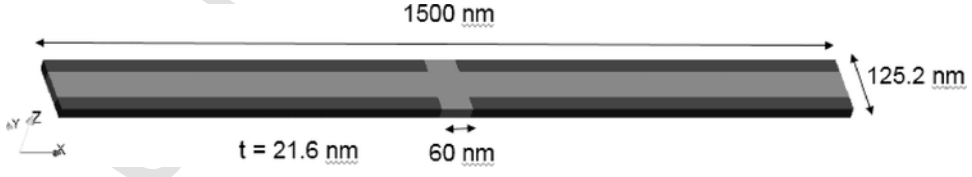

Fig. 9. Plate-like design crux2D of crystalline/amorphous lamella. The total width of the crystalline phase (dark color) is set to 60 nm, whereas the width of amorphous phase (grey color) is 65.2 nm, according to the crystallization degree $\xi = 53\%$.

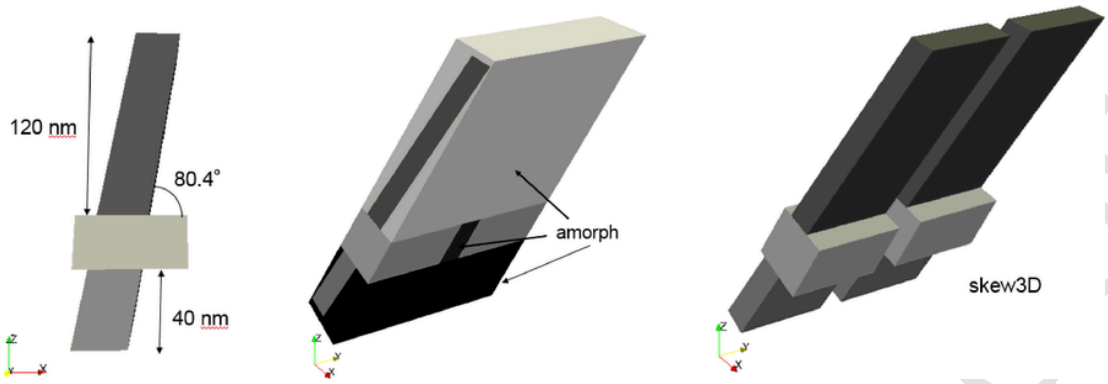

Fig. 10. RVE design skew3D with forward and backward branches. Left: definition of the two branches in the plane $\mathbf{E}_1$–$\mathbf{E}_3$. Middle: whole RVE with amorphous phase enveloping the crystalline branches. In light grey is represented in the right figure the primary growing crystalline lamella.

observation of Li et al. (1999): branches in growth direction are nearly four times longer than secondary branches in backward direction, due to limited material supply because most of the molecular chains are trapped by adjacent lamellae. The design skew3D has the same crystallization degree as design crux2D. The secondary branches have been skewed by an angle of 45° in the plane $\mathbf{E}_2$–$\mathbf{E}_3$ (see Fig. 7 right), perpendicular to the growth direction $\mathbf{E}_1$, as shown in Fig. 10 right. Thus, directions $\mathbf{E}_2$ and $\mathbf{E}_3$ play the same role; whereas without skewing, direction $\mathbf{E}_3$ becomes stiffer as the branching angle lies in the plane $\mathbf{E}_1$–$\mathbf{E}_3$. Moreover, in contrast to the design crux2D, the whole crystalline phase is enveloped by the amorphous phase, so that 3D periodic boundary condition can be specified on the RVE.

With the Hooke matrices (15) and (16) for the amorphous and crystalline phases respectively, we obtain by asymptotic homogenization for both lamella designs following effective Hooke matrices (in MPa) of the α-iPP lamella in the local axis system ($\mathbf{E}_1$, $\mathbf{E}_2$, $\mathbf{E}_3$):

$$H^{eff}_{crux2D} = \begin{bmatrix} 3277 & 1888 & 1871 & 0. & -76.3 & 0.005 \\ & 2148 & 1923 & 0. & 63.7 & -0.003 \\ & & \mathbf{8747} & -0.003 & -82.2 & 0. \\ & S & & 24.75 & 0. & -1.07 \\ & & Y & & 660.0 & -0.03 \\ & & & M & & 33.18 \end{bmatrix};$$

$$H^{eff}_{skew3D} = \begin{bmatrix} 3048 & 1790 & 1853 & -1.30 & -28.4 & 3.21 \\ & 2120 & 1791 & 2.30 & 120.5 & 16.97 \\ & & \mathbf{7522} & 0.56 & 16.55 & 48.72 \\ & S & & 509.1 & 17.85 & 9.17 \\ & & Y & & 573.0 & 2.28 \\ & & & M & & 680.3 \end{bmatrix}$$

The effective Hooke matrix of design crux2D is *quasi monoclinic* and presents a pronounced anisotropy due to the folded chain oriented in direction $\mathbf{E}_3$ in the crystalline phase. Compared to the pure crystalline phase one, this anisotropy is reduced. The effective Hooke matrix of design skew3D is *full anisotropic*. In Table 1 the effective Young and shear modules for both designs of the α-iPP lamella, expressed in the local axis system ($\mathbf{E}_1$, $\mathbf{E}_2$, $\mathbf{E}_3$), are outlined. As the crystallization degree ($\xi = \_53\%$) is identical for both lamella designs, *the volume averaging Hooke matrix*, corresponding to the 1st term of Eq. (25), *is the same for both designs*. The deduced Young and shear modules are reported also in Table 1. For each design, they allow to quantify the accuracy increase due to the 1st order homogenization correction terms via Eq. (25).

Table 1
Effective Young and shear modules [MPa] of both lamella designs crux2D and skew3D in the local axis system and the corresponding volume averaging values.

Design	E_1	E_2	E_3	G_{12}	G_{13}	G_{23}
crux2D	1615.85	968.57	**6997.79**	***25.17***	649.53	***29.94***
skew3D	1657.24	1260.51	**6029.75**	508.38	558.17	679.81
vol. avrg.	1831.97	1356.50	7331.14	647.88	648.34	758.12

Design crux2D predicts stronger stiffness in folded chain direction $\mathbf{E}_3$ than the design skew3D due to the absence of an amorphous/crystalline interface with a normal in $\mathbf{E}_3$ direction. Due to its construction with a skew angle of 45° in the plane $\mathbf{E}_2$-$\mathbf{E}_3$, design skew3D provides also a larger Young modulus E_2 than design crux2D, so that *the overall anisotropy of the equivalent lamella is reduced mainly in* $\mathbf{E}_2$ *and* $\mathbf{E}_3$ *directions:*

- skew3D: $\Delta E_{1,m} = -44.4\%$; $\Delta E_{2,m} = -57.7\%$; $\Delta E_{3,m} = 102.2\%$ with $E_m = 2982.5$ MPa
- crux3D: $\Delta E_{1,m} = -49.4\%$; $\Delta E_{2,m} = -69.7\%$; $\Delta E_{3,m} = 119.1\%$ with $E_m = 3194.1$ MPa

with deviation definition: $\Delta E_{i,m} = \left(E_i - E_m\right)/E_m$

The predicted effective shear modules confirm the reduced global anisotropy of design skew3D against the design crux2D: maximum deviation $\Delta G_{23,skew} = 16.8\%$ against $\Delta G_{13,crux} = 176.5\%$! Indeed, only 2D periodic boundary conditions (B.C.) are applied in the plane $\mathbf{E}_1$–$\mathbf{E}_2$ of RVE crux2D, out-of-plane displacements become large, inducing unphysical, large corrections to the volume averaging values via expression (25). Therefore, *design skew3D outperforms design crux2D not only physically, due to modeling of observed secondary branches in a spherulite, but also numerically*.

4.5. Homogenization of a polyspherulite microstructure

At the microscale, the objective is to predict the effective mechanical properties of polyspherulite microstructures, predicted by SphaeroSim by using the 3D crystallization model, described in Section 3. The homogenization tool HOMAT reads the final solidified microstructure (see Fig. 2 and 11 left) and needs two additional ingredients to perform their homogenization:

- *The 3D radial spherulite model* to describe accurately the equivalent behavior of each spherulite individually;

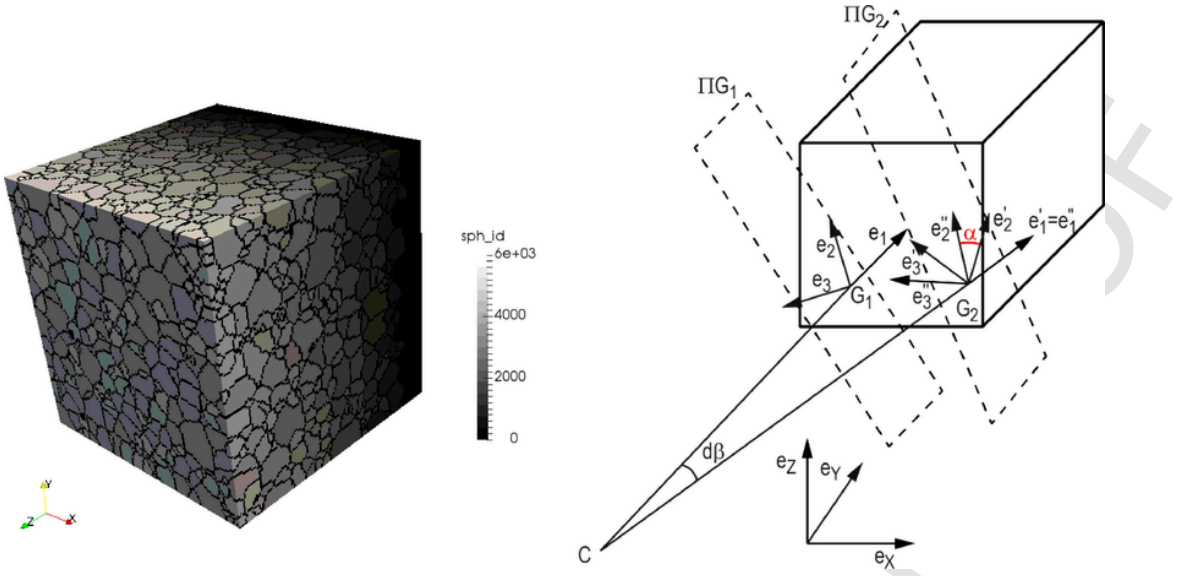

Fig. 11. Left: Spherulite microsture calculated by SphaeroSim and located at the top skin in the 3 mm section of the staggered α-iPP plate. Right: Definition of the local axis system ($\mathbf{e}_1$, $\mathbf{e}_2$, $\mathbf{e}_3$) in Gauss point G_1 and ($\mathbf{e}_1$", $\mathbf{e}_2$", $\mathbf{e}_3$") in Gauss point G_2.

- The mechanical properties of the thin boundary layer between spherulites. In the present work, this thin layer is considered firstly as an individual phase and is discretized with a thickness of one cell in Fig. 11.left.

(A) *The 3D radial spherulite model*: The effective lamella is distributed radially around the spherulite center in practice as follows: in each Gauss point of the finite element discretization, the normalized vector $\mathbf{P}_G$ **- C** is expressed (see Fig. 11.right). This vector defines the growth direction of the crystalline/amorphous lamella and corresponds to the direction $\mathbf{e}_1$ of the local lamella axis system.

As currently no reliable experimental information exists on how the crystalline lamella is oriented in the plane perpendicular to its growth direction, the local directions $\mathbf{e}_2$ and $\mathbf{e}_3$ are specified randomly in the 1st Gauss point of a spherulite. In order to improve the initial model (Laschet et al, 2012), the directions in the next Gauss points are expressed now in a *deterministic* way rather randomly as physically there exists an unknown orientation relationship between neighborhood lamellas:

- At first, the growth directions $\mathbf{e}_1$ and $\mathbf{e}_1$' of the Gauss points G_1 and G_2 (see Fig. 11.right) are expressed in spherical coordinates (r, θ, φ) respectively. Then a rigid body rotation of the local axis system ($\mathbf{e}_1$, $\mathbf{e}_2$, $\mathbf{e}_3$) of Gauss point G_1 to Gauss point G_2 is achieved, defining thus the intermediate, local system ($\mathbf{e}_1$', $\mathbf{e}_2$', $\mathbf{e}_3$'). Angle dβ specifies this rotation:

$$d\beta = \sqrt{(\theta_2 - \theta_1)^2 + (\varphi_2 - \varphi_1)^2} \tag{27}$$

- In the perpendicular plane Π_{G2} defined by the intermediate unit vectors $\mathbf{e}_2$' and $\mathbf{e}_3$' (see Fig. 11.right) *an additional rotation* α is then applied around the common normal $\mathbf{e}_1$' = $\mathbf{e}_1$". Different coarse and fine discretizations of an idealized spherulite with central nucleus have shown that this angle has to be specified in the range α ∈ [65°–85°] in order to get a quasi-isotropic elastic equivalent behavior of the idealized spherulite. This angle varies linearly within its validation range with the distance of the considered Gauss point G_i to the spherulite center **C** via expression:

$$\alpha = 65^\circ + \left(\frac{|\mathbf{P}_{Gi} - \mathbf{C}|}{|\mathbf{P}_{Gmax} - \mathbf{C}|} \right) \times 20^\circ \tag{28}$$

where $\mathbf{P}_{Gmax}$ is, for each spherulite, the largest distance to its center.

This way, we take into account the twisting of the lamella in the 3D spherulite and the local axis system ($\mathbf{e}_1$", $\mathbf{e}_2$", $\mathbf{e}_3$") in the considered Gauss point G_i is specified in a deterministic manner.

Then, the Hooke matrix of the equivalent lamella, expressed in the local axis system of each Gauss point, is rotated to the original RVE axis system ($\mathbf{e}_X$, $\mathbf{e}_Y$, $\mathbf{e}_Z$), which has been chosen parallel to the structural axis system of the injection molding process (see Fig. 11). Note that at a larger distance from the spherulite center, the number of Gauss points in the spherulite increases also. Thus, the nucleation of secondary or tertiary branches of lamella in the spherulite is taken implicitly into account by the specification of more Gauss points at a certain distance from the spherulite center than nearby. In each Gauss point, a lamella with its own orientation, defined by Eqs. (27) and (28), is assumed to be located there. Moreover, the subsequent asymptotic homogenization calculation takes via the implicit body forces $\mathbf{g}^{\Delta H}$ (see eq. 24) *the variation of the lamella orientation within each spherulite* into account. This is an advantage of the developed homogenization scheme.

(B) *The spherulite boundary (SB)* is considered here as an individual isotropic phase dotted with its own elastic properties. As presently there is no experimental characterization of the spehrulite boundary available in the literature, their specification is delicate. Here a residual degree of crystallization of ξ_{SB} = 33% is assumed due to the fact that in reality folded molecule chains end in the thin boundary layer. Applying a simple mixture rule, we get following elastic properties: $E_{SB} = \xi_{SB} E_{crys,m} + (1 - \xi_{SB})\, E_a = 1065.5\,\text{MPa}$ and $\nu_{SB} = \xi_{SB} \nu_{crys,m} + (1 - \xi_{SB})\, \nu_a = 0.4733$.

5. Application: multiscale simulation of an injection molded step plate of α-iPP

As an example of the developed integrative simulation chain, the injection molding process of a staggered plate made of isotactic polypropylene type 505P, SABIC AG, Bergen op Zoom, Netherlands, is considered here. The geometrical configuration of the stepped component, designed for a welding application, is given in Fig. 12. It has been selected because it has different thicknesses ranging from 1 mm to 4 mm. In each of the stairs different cooling and flow conditions exist, which affect the formation of the spherulite microstructures directly and thus also the mechanical properties in each step. A comprehensive characterization of the macroscopic thermophy-sical properties of this α-iPP can be found in Spina et al. (2014b). To calculate the microstructure dependent effective elastic properties of injection molded parts, a multi-scale simulation chain of three simulation tools has been set up, which operate at three distinguish scales: macro-, micro- and nanoscale.

5.1. 3D mold filling and heat transfer analysis

Real process parameters are adopted for the 3D coupled mold filling and transient heat transfer simulation with the multiphysics FE code COMSOL: an inlet flow of 25 cm^3/s, a pressure level of 70% of the maximum injection pressure of 120 MPa, a pressure time of 20 s and a cooling time of 40 s. The mold wall temperature was set to 40 °C; whereas a melt temperature of 220 °C has been adopted. To compute accurately the filling progress P2 + P1 Taylor–Hood elements with quadratic shape functions for the velocity field and the free surface field, ϕ and linear functions for the pressure and temperature fields are used. The mesh size of the mold cavity used in the mold filling analysis was 100 μm.

The 3D melt front in section S3 is shown in Fig. 13. As each plate stair has a uniform cross-section, a steady state velocity profile was

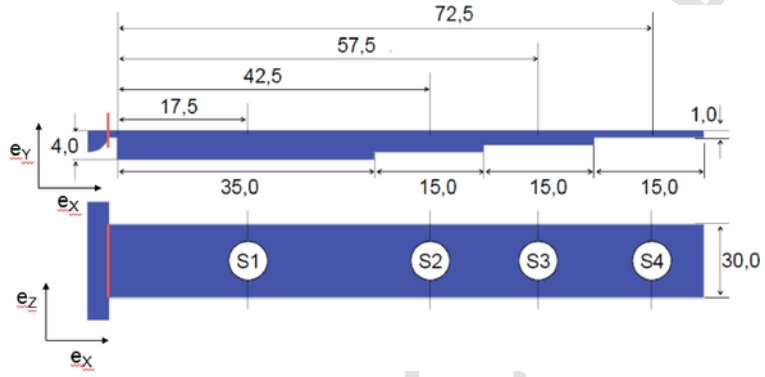

Fig. 12. Geometrical configuration of the 505P polypropylene staggered plate.

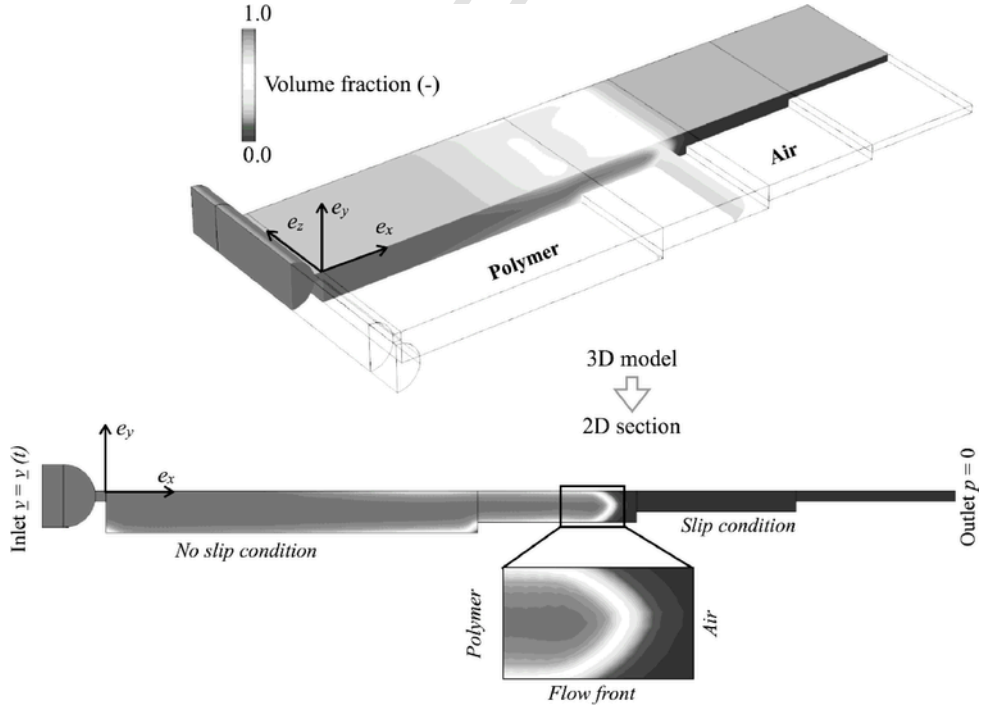

Fig. 13. Flow front advancement in the stepped α-iPP plate for a given inlet velocity and zero outlet pressure.

developed after a short transient time. The obtained velocity profile points out that the polymer melt undergoes a fountain flow effect with a higher velocity at the centerline than at both mold walls, The flow front is not pure symmetrical but slightly shifted to the upper mold wall as the flow entrance is near this wall. In addition to the velocities and the position of the flow front, the temperature distribution is also necessary for the calculation of the solidification process. The temperature increases at the mold wall during the filling and the holding phase from 40 °C to 50 °C. The temperature profile in the middle plane of the staggered plate is shown in Fig. 14 and is induced by different heat fluxes at the steel walls and at the filling front. The polymer in contact with both mold walls freezes rapidly due to the high local thermal gradient, creating thus a thin insulating layer and inducing a quasi-constant temperature in the core; whereas the air/melt heat flux cooled the melt but not enough to solidify the melt.

5.2. Microstructure evolution simulation

As illustrated in Fig. 11 four cross sections have been defined in the middle of each stair of the plate. The crystallization process is predicted at the microscale in each of these cross sections. In the 3 mm section 10 RVE's of extension 300 μm^3 are defined over the cross section thickness. They are all located in the middle of the Z axis. Each cubic RVE is discretized by 120 cells per direction, leading to a model with 1728,000 cells. Thus, each RVE cell has an extension of 2.5 μm^3. The 2 mm section is discretized by 7 RVE's of same extension over its thickness, except the central one with an extension of 300*200*300 μm^3. These RVE's are also located in the middle of the Z axis (Z = 15 mm).

Fig. 15 left shows the microstructure over the cross-section at section S3 within the light microscope. A fine structured layer is observed in the core, which is surrounded by two layers with larger spherulite diameters. Two fine structured layers appear at the mold wall. They are the result of the steep cooling gradients; whereas the interplay of flow and temperature results in the structure of the other layers. The microstucture evolution during solidification in the five observed layers is also predicted with the developed in-house tool SphaeroSim (see Fig. 15 right). The expected solidification progress from the mold wall to the core occurs throughout the entire crystallization process. The core area solidifies within a few seconds resulting in a finer structure. The predicted diameters are in a range up to a diameter of 32 µm, which is in agreement to the observation (see Fig. 16).

Fig. 17 shows the solidified spherulite microstructure in the core area at section S2. Again, the calculated diameters of 40 µm are in good agreement to the corresponding micrograph.

Moreover, this good agreement can be confirmed by comparing spherulite diameters at different positions over the wall-thickness

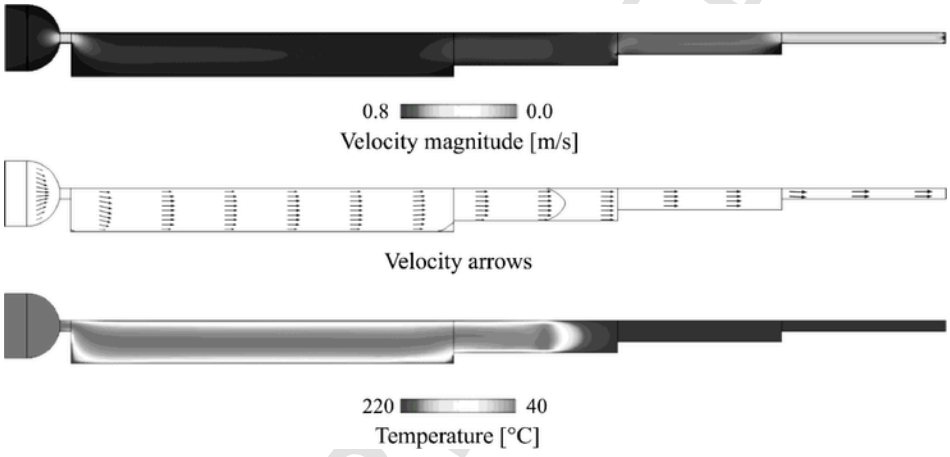

Fig. 14. 2D temperature and velocity profiles in the middle plane (Z = 15 mm) of the α-iPP plate.

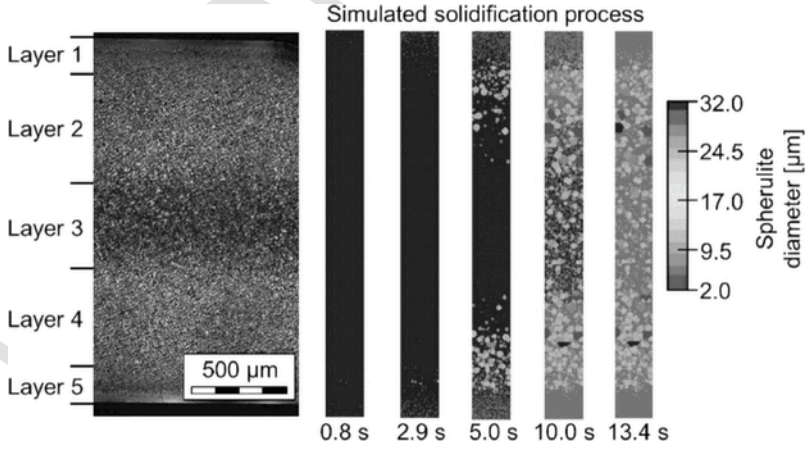

Fig. 15. Left: polarized light microscopy of section S3: Right: microstructure evolution during solidification. The predicted five layer structures are also observed experimentally in the microscopy image.

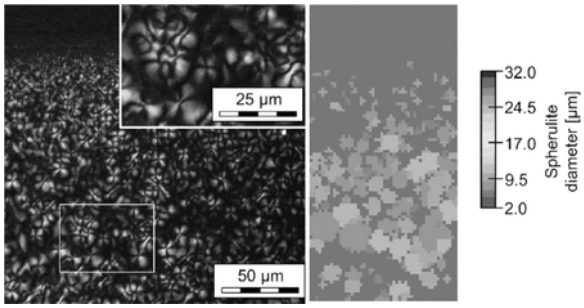

Fig. 16. Comparison of the spherulite diameter close to the mold wall at section S3.

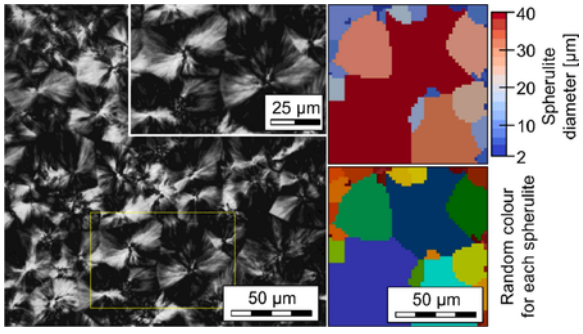

Fig. 17. Comparison of the spherulite diameter in the core area of section S2. To distinguish the different spherulites a random color has been assigned to each one, which is shown in the bottom right.

(see Fig. 18) with computed results of the macro- and micro-models. In particular the values closer to the mold walls are computed at 1.0 s at locations S2 and S3.

The variation of the spherulite diameters is a direct result from the temperature and velocity fields, which change over the wall-thickness. The experimental validation of the microstructure simulation was only done for the spherulite diameter because it is directly accessible via polarized light microscopy figures of thin cuttings. Other quantities like the volume fraction of the spherulites or its total number require indirect measurement techniques which usually require further extrapolations or crystallization models itself.

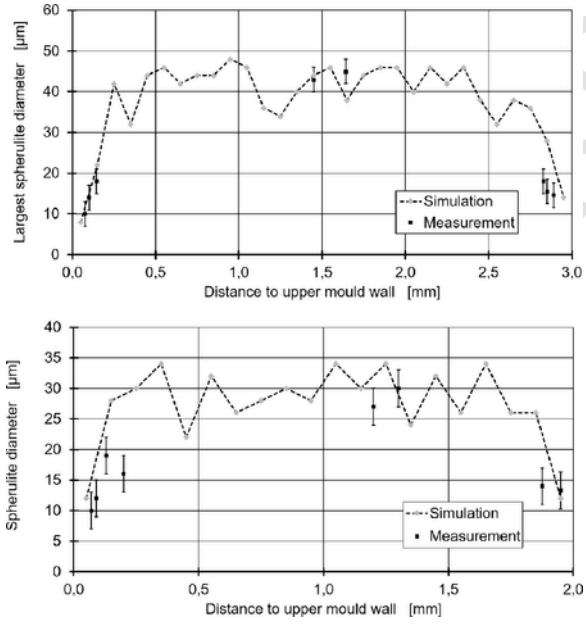

Fig. 18. Comparison of the spherulite diameters of section S2 (3 mm) and S3 (2 mm).

For each location over the cross sections 2 and 3 mm the solidified microstructure is transferred to the homogenization program HOMAT. Note that in both plate sections, both extremal RVE's in direct contact with the mold wall are not transferred as their microstructure is very fine with a lot of spherulites having only one cell extension! In the VTK exchange files the spherulites and their boundaries are written and in a separate file, the center of each spherulite.

5.3. Prediction of effective elastic properties

At first, the cellular automaton cells are converted to linear hexahedron elements and 2D periodic BC in directions $\mathbf{e}_X$ and $\mathbf{e}_Y$ are applied on all RVE's of sections S2 and S3 to perform the asymptotic homogenization analyses. The effective elastic properties of both lamella designs, crux2D and skew3D, are retained in the homogenization runs in order to quantify their impact on the overall effective properties of the α-iPP plate. The predicted effective Young modulus in the flow direction, E_X, is drawn over the thickness of section S3 for both lamella variants in Fig. 19. The experimentally measured Young modulus of a PP plate of thickness 3 mm, $E_{exp} = 1721$ MPa is outlined as reference. The predictions of the design skew3D are obviously closer to the experimental value than the predictions of design crux2D. Indeed, only a maximum deviation of ***1.38%*** is noted for the RVE located at Y = −1.95 mm; whereas design crux2D induces a maximum deviation of ***−14.01%*** for the RVE located at the top plate skin (Y = −0.45 mm). This result underlies that the lamella design skew3D outperforms the crux2D one. Therefore, a detailed analysis has been achieved only for design skew3D.

At Fig. 20, the variation of the predicted effective modules in the structural axis system is given for both plate sections S2 and S3. The 2-level homogenization scheme predicts *an orthotropic equivalent behavior in both plate sections* with always $\mathbf{E_Y < E_X < E_Z}$. Likewise, this anisotropy tendency is corroborated by the experimentally measured mean Young modules in the flow direction, $E_{x,\,exp}$ and in the thickness direction Z, $E_{z,exp}$ for the plate section S3. Note that later Young modulus is derived from an acoustic experiment via reverse engineering. Moreover, *a significant asymmetry behavior over the plate thickness is predicted in both sections.* The Young mod-

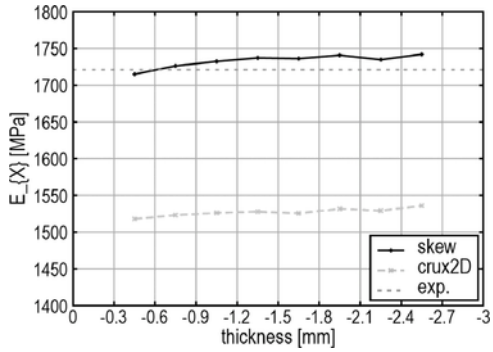

Fig. 19. Effective Young modulus E_X in flow direction, predicted by designs crux2D and skew3D, and the experimentally measured Young modulus.

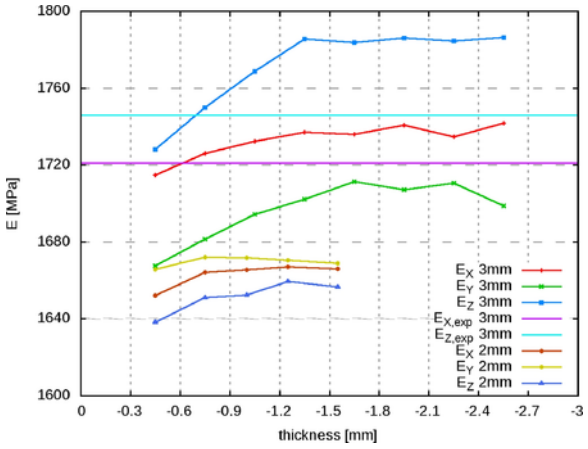

Fig. 20. Variation of the effective Young modules over the thickness of sections S3 and S2 predicted with lamella design skew3D.

ules at the top plate skin are smaller, thus inducing a locally more flexible behavior, than the modules predicted at the other skin. This different local stiffness over the plate sections S2 and S3 can be explained by the different cooling behavior at the two mold walls (see Fig. 21) and the resulting microstructure variations. Indeed, at the top skin the cooling gradient is high, leading to a significant undercooling; whereas at the bottom skin with its steps, not only the gradient is lower but also, due to melt flow recirculation, the polymer is reheated before it solidifies. This different cooling behavior induces not only different microstructures at top and bottom mold walls but also a stiffer elastic behavior at the bottom skin. The local re-heating identified in both curves was caused by the release of the latent heat of crystallization ΔH_C (see Eq. (3)) during the crystallization process.

The comparison of the variation of the Young modules over sections S2 and S3 indicates clearly that *section S2 presents lower overall stiffness than section S3 due to its finer spherulite microstructure*. Indeed, as shown in Fig. 22, due to stronger cooling in section S2 the number of spherulites per volume unit in each RVE is there larger than in section S3. This finer microstructure induces a significant increase of the spherulite boundaries, as shown in Fig. 22 right:

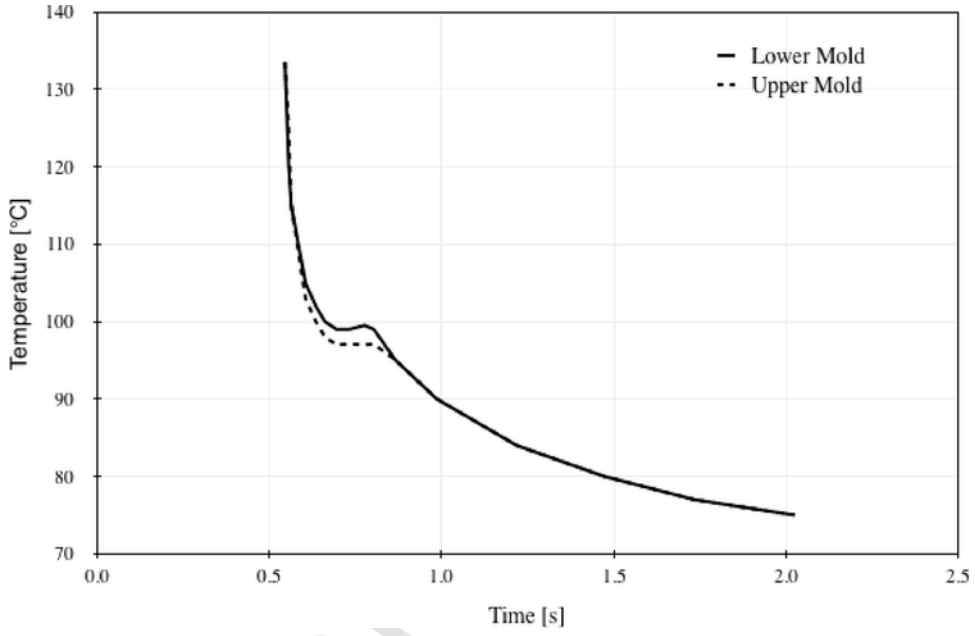

Fig. 21. Cooling curves in section S2 at two points P1 and P2 near both mold walls.

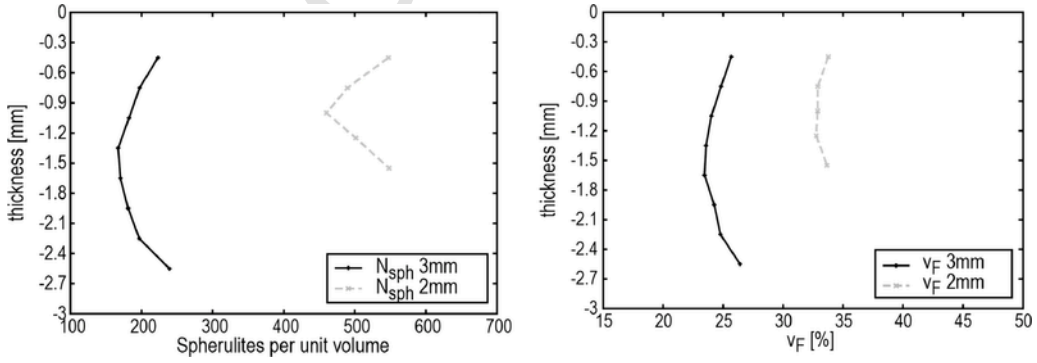

Fig. 22. Left: number of spherulites per unit volume [100 μm^3] in sections S2 and S3. Right: volume fraction of spherulite boundaries in the RVE's defined over the thickness of sections S2 and S3.

$V_{f,SB}$ varies around 33.2% in section S2; whereas it varies around 24.6% in section S3. As the spherulite boundary is weaker than a spherulite itself, it is obvious that the homogenization runs predict a more flexible behavior of the 2 mm section than of the 3 mm one.

Important is to comment the anisotropic effect of the above results. The different cooling and flow conditions in sample points lead to different nucleation and growth speeds so that the number of spherulites and their shape are very different near both tool walls and in the plate center. Moreover, in the investigated stepped preform the upper and lower walls present also different cooling behavior (see Fig. 21). Therefore, local variations of mechanical properties over the plate cross sections are expected. The homogenization analysis evaluates the effective properties of 10 RVE's (section S3) or 7 RVE's (section S2) over the plate thickness respectively and determines for each of them its specific anisotropy. The origin of the anisotropy lies clearly in the mechanical behavior of the crystalline phase of i-αPP: the folded molecular chain of helicoidal type. Its Hooke matrix (see Eq. (16)) is monoclinic and presents a strong anisotropy. Therefore, independent of the adopted design (with or without secondary branches), the effective properties of the lamella are anisotropic. Moreover, at the RVE level, implicit surface tractions are generated at the spherulite boundaries between adjacent spherulites and volume forces due to the Hooke matrix variation within each spherulite, induced by different lamella orientation in each Gauss point (see Fig. 11). These forces (see Eq. (24)) induce microscopic displacement and strain fields on each RVE, which are used in the evaluation of the effective Hooke matrix (see Eq. (25)) and are responsible for the anisotropy of each calculated RVE over the plate cross sections.

The effective shear modules, outlined in Fig. 23 left, corroborate the Young modules results: section S2 is more flexible than section S3 and a pronounced orthotropic equivalent behavior with $\mathbf{G_{XY} < G_{YZ} < G_{XZ}}$ is predicted. An asymmetric variation of the shear modules over both cross sections is also observed. Otherwise, independent of the shear plane, the corresponding modulus is slightly larger in the center of the cross sections than at both skins. Eventually, the effective Poisson coefficients are draw in Fig. 23 right over the thickness of sections S3 and S2 respectively. Poisson coefficients ν_{XZ} and ν_{YZ}, having transverse direction Z in common, are quite similar and their values are much larger than the in plane Poisson coefficient ν_{XY}, whose mean value is 0.333 in section S3 and 0.3365 in section S2. The mean values of ν_{XZ} are 0.457 (S2) and 0.441 (S3) and of ν_{XZ} are 0.456 (S2) and 0.449 (S3) respectively. Due to finer microstructure with a larger spherulite boundary, the impact of the incompressible amorphous phase is more pronounced in section S2 than in section S3, explaining so the slightly larger mean values in section S2 than in section S3.

6. Conclusions

An integrative, multiscale simulation approach for the derivation of inhomogeneous mechanical properties in semi-crystalline polymer components has been presented and successfully applied to the mold injection of a stepped α-iPP plate. The boundary conditions for the crystallization process were calculated using a multiphase filling and cooling simulation. A crystallization model was implemented on the macro- and micro-scale to predict the changes of crystallization degree and the evolution of spherulite (nucleation and growth) during cooling. Both quiescent and shear-induced crystallization were computed and validated with experimental data. The application of the step plate shows that a COMSOL - SphaeroSim link is able to predict the effects of process parameters on the spherulite's morphology and their predicted diameters are correct. In the subsequent homogenization step, a dedicate two-level homogenization scheme has been extended successfully. Indeed, the crimping of the crystalline molecular chain, the twisting of the lamellae and the possible formation of branches due to secondary nucleation are taken firstly in the design of the lamella into account. This two-level homogenization scheme allows the accurate determination of the influence of the lamella design and of the crystalline properties on the effective properties of spherulitic microstructures. In the 3D radial spherulite model, the definition of the lamella orientations perpendicular to the radial growth direction has been revisited: these orientations are specified only in the 1st discretization point randomly; whereas in all other points they are expressed in a deterministic way. The concept of an interface boundary between spherulites as independent isotropic phase has been introduced. The developed multiscale approach allows to derive microstructure dependent inhomogeneous material properties in injection molded parts. The orthotropic results are in the range of expected values. Moreover, this investigation shows the importance of the process-related temperature field on the microstructure formation and, subsequently, on the asymmetrical variation of effective mechanical properties in sections of the analyzed staggered α-iPP plate. The calculation of elastic properties of injection molded parts made of PP is seen as a possible application field. However, the models are physical motivated and allow a direct transfer to other processing methods, like extrusion. Thus, the application domain becomes larger.

In future work, the presented integrative multiscale scheme will be extended to derive effective thermal properties and the effective viscoplastic behavior of α-iPP. Moreover, in analogy to the method suggested by Boettger et al. (2009) for metals, an iterative, self-consistent scheme will be developed in order to use not only

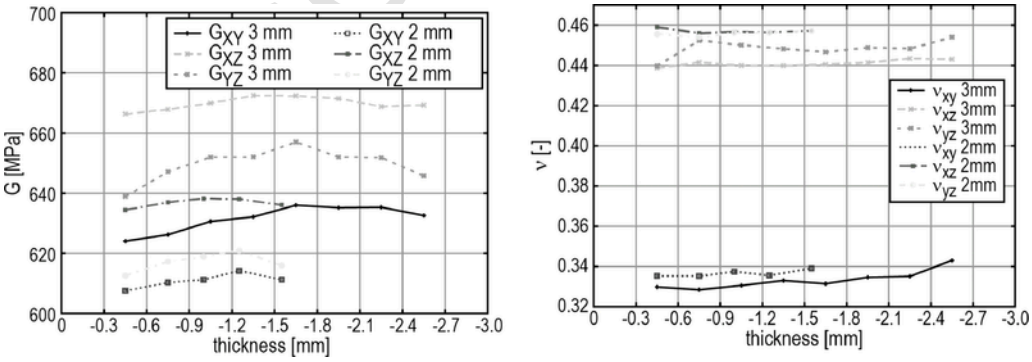

Fig. 23. Variation of effective shear modules and Poisson coefficients over the thickness of sections S3 and S2 predicted with lamella design skew3D.

the predicted effective properties in the mold filling and heat transfer analysis but also to correlate the heat release at the micro- and macro-scale. In addition, an adaptation of the lamella model to the specific characteristics of other semi-crystalline polymers, as HDPE, PET and PLA, will be a subject of future researches.

Acknowledgments

This research was funded by the Deutsche Forschungsgemeinschaft (DFG) as part of the Cluster of Excellence "Integrative Production Technology for High-Wage Countries". The authors wish to thank Peter Hul (ACCESS e.V.) for the mesh generation of the lamella designs and Simon Koch (Institute for Plastics Processing) for its precious support during the research activities.

References

Assoiline, E., Wachtel, S., Grigull, S., Lustiger, A., Wagner, H.D., Marom, G., 2001. Lamellar twisting in α polypropylene transcrystallinity investigated by synchrotron micro-beam X-ray diffraction. Polymer 42, 6231–6237.

Bédoui, F., Diani, J., Régnier, G., Seiler, W., 2006. Micromechanical modelling of isotropic elastic behavior of semicrystalline polymers. Acta Mater. 54, 1513–1523.

Boettger, B., Eiken, J., Apel, M., 2009. Phase-field simulations of microstructure formation in technical castings - a self consistent homo-enthalpic approach to the micro-macro problem. J Comput. Phys. 228, 6784–6795.

Brusselle-Dupend, N., Cangémi, L., 2008. A two-phase model for the mechanical behavior of semi-crystalline polymers. Part I: large strains multiaxial validation on HDPE. Mech. Mater. 40, 743–760.

Castelein, G., Coulon, G., G'Sell, C., 1997. Polymers under mechanical stress: Deformation of the nanostructure of isotactic polypropylene revealed by scanning force microscopy. Polym. Eng. Sci. 37 (10), 1694–1701.

Charbon, C., Swaminarayan, S., 1998. A multicale model for polymer crystallization - II solidification of a macroscopic part. Polym. Eng. Sci. 38 (4), 644–656.

COMSOL, 2014. version 5.0, 2014. https://www.comsol.de/release/5.0

Coppala, S., Grizzuti, N., Maffettone, P.L., 2001. Microrheological modeling of flow-induced crystallization. Macromolecules 34 (14), 5030–5036.

Doi, M., Edwards, S.F., 1988. The Theory of Polymer Dynamics. Oxford University Press.

Fetters, L.J., Lohse, D.J., Colby, R.H., 2007. Chain dimensions and entanglement spacings. In: Mark, J. (Ed.), Physical Properties of Polymers Handbook, second ed.. pp. 447–454. Chapt. 25.

Guedes, J.M., Kikiuchi, N, 1999. Preprocessing and postprocessing for materials based on the homogenization method with adaptive finite element methods. Comput. Meth. Appl. Mech. Eng. 83, 143–198.

Gueguen, O., Ahzi, S., Makradi, A., Belouettar, S, 2010. A new three-phase model to estimate the effective elastic properties of semi-crystalline polymers: application to PET. Mech. Mater. 42, 1–10.

Hoffman, J.D., Davis, G.T., Lauritzen, J.I.Jr., 1976. The rate of crystallization of linear polymers with chain folding. In: Hannay, N.B. (Ed.), Treatise on Solid State Chemistry, Vol. 3. Plenum Press, New York, pp. 497–614.

Ivanov, D., Lomov, S., IvanovS., VerpoestI., 2010. Stress distribution in outer and inner plies of textile laminates and novel boundary conditions for unit cell analysis. Composites: Part A 41, 571–580.

Janeschitz-Kriegl, H., 2010. Crystallization Modalities in Polymer Melt Processing. Springer Verlag, Wien, Austria.

Koscher, E., Fulchiron, R., 2002. Influence of shear on polypropylene crystallization: morphology development and kinetics. Polymer 43 (25), 6931–6942.

Laschet, G., Apel, M., 2010. Thermo-elastic homogenization of a 3-D steel microstructuresimulated by the phase-field method. Steel Res. Int. 81, 637–643.

Laschet, G., Kashko, T., Benke, S., Öte, M., Bobzin, K., 2012. Prediction of effective properties. In: Schmitz, G.J., Prahl, U. (Eds.), Integrative Computational Materials Engineering – Concepts and Applications of a Modular Platform. Wiley-VCH, Weinheim, pp. 81–115. Chapter 5.

Lauritzen, J.I., Hoffmann, J.D., 1960. Theory of formation of polymer crsytals with folded chains in dilute solution. J. Nat. Bur. Stand. 64A (1), 73–102.

Lee, B.J., Parks, D.M., Ahzi, S., 1993. Micromechanical modelingof large plastic deformation and texture evolution n semi-crystalline ploymers. J. Mech. Phys. Solids 41 (10), 1651–1687.

Lee, O., Kamal, M.R., 1999. Experimental study of post-shear crystallization of polypropylene melts. Polym. Eng. Sci. 39 (2), 236–248.

Li, L., Chan, C.M., Yeung, K.L., Li, J.X., Ng, K.M., Lei, Y., 2001. Direct observation of growth of lamellae and spherulites of a semi-crystalline polymer by AFM. Macromolecules 34, 316–325.

Mahnken, R., Caylak, I., Laschet, G., 2008. Two mixed finite element formulations with area bubble functions for tetrahedral elements. Comput. Meth. Appl. Mech. Eng. 197, 1147–1165.

Michaeli, W., Hopmann, C., Bobzin, K., Arping, T., Baranowski, T., Heesel, B., Laschet, G., Schläfer, T., Oete, M., 2012. Development of an integrative simulation method to predict the microstructural influence on the mechanical behavior of semi-crystalline thermoplastic parts. Int. J. Mat. Res. 103 (1), 120–130.

Mischler, G, Baltra-Calleja, F, 2012. Nano- and Micromechanics of Polymers. Hanser Verlag GmbH & Co. KG, München, Germany.

Nakurama, K., Katayama, K., Amato, T, 1973. Some aspects of nonisothermal crystallization of polymers. II. Consideration of the isokinetic condition. J. Appl. Polym. Sci. 17 (4), 1031–1041.

Nemat-Nasser, S., Hori, M., 1999. Micromechanics: Overall Properties of Heterogeneous Materials, second ed. North Holland, Netherlands.

Nikolov, S., Doghri, I., Pierard, O., Zealouk, L., Goldberg, A., 2002. Multiscale constitutive modeling of the small deformations of semi-crystalline polymers. J. Mech. Phys. Solids 50, 2275–2302.

Oktay, E., Gürses, E., 2015. Modeling of spherulite microstructures in semicrystalline polymers. Mech. Mat. 90, 83–101.

Olsson, E., Kreiss, G., 2005. A conservative level set method for two phase flow. J. Comput. Phys. 210 (1), 225–246.

Osher, S, Sethian, J.A., 1988. Fronts propagating with curvature-dependent speed: algorithms based on Hamilton-Jacobi formulations. J. Comput. Phys. 79 (1), 12–49.

Pantani, R., Coccorullo, I., Speranza, V., Titomanlio, G., 2005. Modeling of morphology evolution in the injection molding process of thermoplastic plomers. Progr. Polym. Sci. 30 (12), 1185–1222.

Paraview, 2014. version 4.2, 2014. Kitware http://www.paraview.org

Raabe, D., 2004. Mesoscale simulation of spherulite growth during polymer crystallization by use of a cellular automaton. Acta Mater. 52, 2653–2664.

Raabe, D., Godora, A., 2005. Mesoscale simulation of the kinetics and topology of spherulite growth during crystallization of isotactic polypropylene (iPP) by using a cellular automaton. Modell. Simul. Mater. Sci. Eng. 13, 733–751.

Spekowius, M., Spina, R., Hopmann, C., 2016. Mesoscale simulation of the solidification process in injection molded parts. J. Polym. Eng. 36 (6), 563–574.

Spina, R., Spekowus, M., Hopmann, C., 2014. Multi-scale thermal simulation of polymer crystallization. Int. J. Mater. Form.1–8.

Spina, R., Spekowius, M., Dahlmann, R., Hopmann, C., 2014. Analysis of polymer crystallization and residual stresses in injection molded parts. Int. Jnl. Precis. Eng. Manuf. 15 (1), 85–92.

Tashiro, K., Kobayashi, M., Tadoroko, H., 1992. Vibrational spectra and theoretical 3-D elastic constants of isotactic polypropylene crystal: an important role of anharmonic vibrations. Polym. J. 24 (9), 899–916.

Uchida, M., Tokada, T., Tada, N., 2010. Finite element simulation of deformation behavior of semi-crystalline polymers with multi-spherulitic mesostructure. Int. J. Mech. Sci. 52, 158–167.

Uchida, M., Tada, N., 2013. Micro-, meso- to macroscopic modeling of deformation behavior of semi-crystalline polymer. Int. J. Plast. 49, 164–184.

Van Dommelen, J.A.W., Parks, D.M., Boyce, M.C., Brekelmans, W.A.M., Baaijens, F.P.T., 2003. Micromechanical modeling of the elastoplastic behavior of semi-crystalline polymers. J. Mech. Phys. Solids 51, 519–541.

Wienke, S., Spekowius, M., Dammer, A., An Mey, D., Hopmann, C., Müller, S.M., 2013. Towards an accurate simulation of the crystallization process in injection molded plastic components by hybrid parallelization. Int. J. High Perform. Comput. Appl. 28 (3), 356–367.